Near-field turbulent simulations of rectangular jets using lattice Boltzmann method

Huidan Yu[a] and Sharath S. Girimaji[b]
Department of Aerospace Engineering, Texas A&M University, College Station, Texas 77843-3141

(Received 22 March 2005; accepted 11 October 2005; published online 16 December 2005)

We perform large eddy simulation (LES) of the near field of low aspect ratio (AR) rectangular turbulent jets (RTJ) using the lattice Boltzmann method. The computational technique combines a D3Q19 multiple relaxation time (MRT) lattice Boltzmann equation (LBE) with the Smagorinsky model for the subgrid stress. First and foremost, we demonstrate that the MRT-LBE model is more suitable than the widely used single-relaxation-time LBE model for LES of turbulent flows. Then, we proceed to compute four jets with MRT-LBE: AR-1, 1.5, 2, 5; exit velocity u_0 (m/s)-60, 39, 60, 23; and Reynolds number Re-184 000, 25 900, 128 000, 14 000. The investigated near-field behavior includes: (1) Decay of mean streamwise velocity (MSV) and inverse MSV; (2) spanwise and lateral profiles of MSV; (3) half-velocity width development and MSV contours; and (4) streamwise turbulence intensity distribution. The simulation results are compared against experimental data. Two unique features of RTJ—the saddle-back MSV spanwise (major axis) profile and axis switching of major axis from spanwise to lateral direction—are investigated. Our simulations show that the jet statistical behavior is more sensitive to inflow velocity and less so to the transverse boundary conditions. Overall, this work demonstrates that the MRT-LBE method is a potentially reliable computational tool for LES of turbulence even at high Reynolds numbers.
 [DOI: 10.1063/1.2140021]

I. INTRODUCTION

Jets and plumes can be found in various flows in nature and engineering. In recent years, special attention has been given to jets emerging from noncircular exits due to their enhanced entrainment and mixing properties relative to those of comparable axisymmetric jets (Ref. 1 and references therein). Rectangular turbulent jet (RTJ) combines the variable aspect-ratio (AR) feature of elliptic jet with the corner vertex feature of square jet.[2–18] In general, the mixing process in jet shear layers occurs in two stages: initial bulk mixing or large-scale stirring, and subsequent small-scale mixing characterized by gradient steepening leading to enhanced molecular diffusion. The first stage is driven by the generation of large coherent structures that entrain large pockets of ambient fluid. Then, these large-scale fluctuations cascade down to the small scales creating steep gradients which accelerate mixing at the molecular level.

Experimental and analytical investigations[2,3,8] reveal that a RTJ flow field is characterized by the presence of three distinct regions: (i) PC (potential core) region into which the mixing initiated at the jet boundaries has not penetrated; (ii) CD (characteristic decay) region where velocity decay and mixing depend on the jet aspect ratio and shape; (iii) AD (axisymmetric decay) region extending to infinity where the velocity field is axisymmetric independent of the jet exit shape. In this paper we will focus on the near-field (PC and CD regions) jet statistics and flow features.

Analytical treatments of noncircular jets have been based on linear stability analysis.[19–21] However, literature on detailed numerical simulations of three-dimensional RTJ flows is very limited. Most numerical simulations have been performed for round or planar jets and very little for noncircular jets. Early numerical computations of RTJs include Grinstein,[22,23] Miller *et al.*,[24] and Wilson and Demuren[25] with emphasis on the vorticity dynamics in the near and midrange fields. Recently, Rembold *et al.*[26] and Feiz *et al.*[27] performed direct numerical simulation (DNS) and large eddy simulation (LES) of RTJs to investigate some aspects of the flow field.

A. Methodology

The lattice Boltzmann method (LBM)[28,29] is a recently developed numerical scheme that solves the lattice Boltzmann equation (LBE) rather than the Navier-Stokes (NS) equation. The Boltzmann equation, in principle, is valid over a wider range of flow physics than the NS equations. In LBM, microscopic fluid physics is simplified to retain only key elements (the local conservation laws and related symmetries) needed to guarantee accurate macroscopic behavior. This leads to potential computational advantages over traditional continuum methods.[30–33] The possible advantages of LBE over NS equations for LES are discussed in Yu, Girimaji, and Luo.[34] Here, we present the salient points.

(1) The availability of nonhydrodynamic variables in LBM system can possibly lead to a more accurate closure for LES of turbulence. Specifically, some memory and nonlocal effects can possibly be incorporated into the subgrid stress constitutive equation.

[a]Electronic mail: h0y5840@aero.tamu.edu
[b]Electronic mail: girimaji@aero.tamu.edu

(2) In SGS (subgrid stress) closures such as the Smagorinsky model (dynamic or otherwise), an accurate estimate of the resolved strain rate is required. In LBM, the strain rate is directly obtained from the nonequilibrium distribution function rather than the approximate finite difference schemes typically employed in NS-based methods. This can lead to important advantages for LBM over NS methods.[34]
(3) The algorithm is easily amenable to massive parallelization permitting efficient computation of very large systems.

Current LBM computations mostly employ the single-relaxation-time (SRT) LBE model[35,36] due to its simplicity. However, it has been demonstrated recently that the multiple-relaxation-time (MRT) LBE model[37–39] has numerical and physical advantages of improved accuracy and stability.[38,40,41]

B. Goals and objectives

The objective of this work is to systematically investigate the near-field mixing features of RTJs and in the process demonstrate the capability of LBM for LES of turbulence at moderately high Reynolds numbers. The various issues investigated are now listed.

- *MRT versus SRT comparison.* By comparing the flow structures and energy spectra obtained from MRT and SRT, we evaluate the advantages of one method over the other for LES applications. After establishing that MRT is more appropriate, we proceed with the RTJ investigation using MRT-LBE.
- *Square jet study.* Three simulations with various combinations of inflow velocity profiles and side boundary conditions are performed. We compare our results with experimental data to understand the effect of inflow velocity and side boundary conditions on jet behavior.
- *Rectangular jet study.* The various investigated near-field behavior include: (1) decay of mean streamwise velocity (MSV) and inverse MSV; (2) spanwise and lateral profiles of MSV; (3) half-velocity width development and MSV contours; and (4) streamwise turbulence intensity distribution. Emphasis is placed on the near-field flow statistics comparisons with experimental data.
- *Flow structure investigation.* We examine jet flow structure, specifically velocity isocontours to understand axis-switching and saddle-back profiles. We attempt to provide physical explanations for these interesting phenomena.

The remainder of this paper is organized as follows. The flow configuration and computational issues are described in Sec. II. Section III introduces SRT and MRT methods and compares their suitability for LES of turbulence. Section IV contains simulation results and discussions. Finally, we conclude with a brief summary in Sec. V.

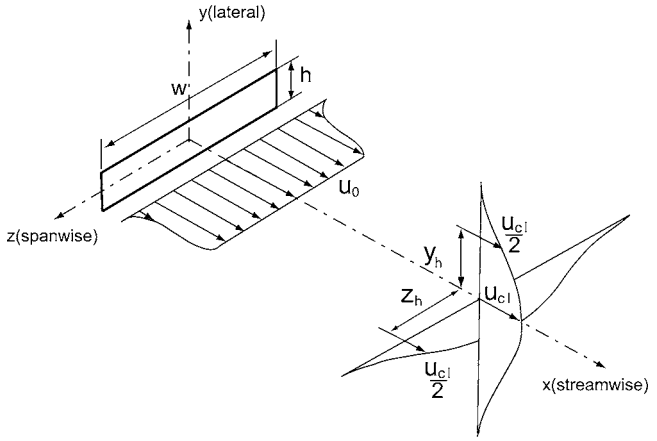

FIG. 1. Schematic configuration and coordinate system of the flow field.

II. FLOW FIELD AND COMPUTATIONAL CONFIGURATIONS

Figure 1 shows the schematic configuration and coordinate system of the flow field with given inflow velocity profile at the jet exit slot. In this figure, the three axes (X—streamwise, Y—lateral, and Z—spanwise), exit velocity (u_0), axis MSV (u_{cl}), jet width (w), height (h), and half-velocity widths (y_h—lateral, z_h—spanwise) are identified. The jet exit major and minor axes are aligned along the spanwise and lateral directions, respectively.

The computational domain of the flow field is a ($W \times H \times L$) channel. The inflow issues from a ($w \times h$) orifice exit. This results in a jet of $\mathrm{AR} \equiv w/h$ and an equivalent diameter of $\mathrm{De} \equiv 2\sqrt{wh/\pi}$. Equivalent diameter is defined as the diameter of a round exit with the same exit area as the rectangular exit. Reynolds number is calculated from jet exit height (h), jet exit velocity (u_0), and viscosity of air (ν). Four jets are computed: one square jet and three rectangular jets of various ARs. The details of these four jets are shown in Table I. The last column in Table I lists the references of corresponding experiments against which we compare our simulation results.

We apply a generalized bounce-back boundary condition[42] at jet exit area ($x=0$, $|z| \leqslant w/2$, and $|y| \leqslant h/2$) and the remainder of the jet exit plane ($x=0$, $|z| > w/2$, and $|y| > h/2$) is treated as a solid wall where $\mathbf{u}_b = 0$. This bounce-

TABLE I. Low AR RTJs conducted in this work

Jet	u_0 (m/s)	$w \times h$ (m^2)	AR ($\equiv w/h$)	D_e (m)	Re	$W \times H \times L$ (m^3)	Reference
I	60	0.01×0.01	1	0.011	184 000	$0.05 \times 0.05 \times 0.28$	11
II	39	0.015×0.01	1.5	0.014	25 900	$0.06 \times 0.037 \times 0.28$	9
III	60	0.026×0.013	2	0.02	128 000	$0.088 \times 0.044 \times 0.3$	12 and 13
IV	23	0.05×0.01	5	0.025	14 000	$0.1 \times 0.042 \times 0.32$	9

TABLE II. Computational grid sizes of the four jets.

Jet	Jet exit	Full domain
I	20×20	$80\times80\times450$
II	24×16	$90\times60\times450$
III	40×20	$140\times70\times450$
IV	70×14	$150\times60\times450$

back scheme can accommodate solid wall and momentum flux boundary conditions. At a solid wall, an incoming particle is bounced back with the same magnitude of momentum. At the jet exit slot, however, any incoming particle is bounced back with added momentum corresponding to the prescribed inflow. The implementation of these boundary conditions can be found in Ref. 41. Fully developed boundary condition is applied at outflow ($x=L$).

A. Computational domain size

The computational domain sizes of all the computed jets are shown in Table II. Our computations are intended to capture potential core and characteristic decay regions ($x<15$De) but not the axisymmetric decay portion. Physically accurate calculation of the axisymmetric decay region will require computational resources beyond the scope of this study.

The computational length along the streamwise direction, however, is longer: $x\simeq25$De. The domain beyond $x=15$ De is called the buffer region and the flow in this part is nonphysical. The need for a buffer region arises from the fact that physically acceptable unsteady and spatially varying outflow condition cannot be easily specified at the physical outflow boundary. Therefore, the buffer region is introduced to gradually damp out the turbulent fluctuations so that the fully developed flow condition can be applied at the computational outflow boundary.

Computations beyond the CD region in literature[11] employ RANS (Reynolds averaged Navier-Stokes equation) models which require substantially lesser computational resources. Further, RANS computations do not need a buffer zone as the flow statistics can be assumed to be fully developed at the outflow boundary. In other jet LES computations, the maximum streamwise extent of the computations is even shorter: $x/\mathrm{De}\leqslant8$ [27] and $x/\mathrm{De}\leqslant10$.[24,25]

While the grid size in the streamwise direction is dictated by the requirement to capture PC and CD regions, the resolution in the transverse plane is chosen after grid resolution studies based on the following considerations:

(1) Grid size must be adequate enough to resolve jet exit geometry.
(2) Grid size must be adequate to resolve important large-scale structures in the PC and CD regions. This is ensured by monitoring the streamwise velocity spectra at various downstream planes. As can be seen in Fig. 6, the MRT spectra at those locations exhibit a steep drop-off at the high wave-number end. This indicates that the resolution is adequate. It is important to point out that the steep decline should not be misconstrued to imply that the subgrid model is unnecessary. Without the subgrid viscosity the simulations become computationally unstable almost instantly.

B. Inflow (jet exit) velocity profiles

It is known that the flow conditions of the jet exit (computational inflow location) play a crucial role in the initial jet development (Refs. 4, 6, 9, 13, 15–17, 24, and 43 and private communication with F. F. Grinstein). Experimental and numerical investigations of RTJs have focused on the influence of jet exit AR,[4,7,13,16,17,24] geometry,[9,15] and flow profiles.[43] In the experiments listed in Table I, Tsuchiya *et al.*[9] uses a uniform laminar streamwise inflow velocity, whereas in the case of Quinn[11,13] the inflow is turbulent with steep gradients in the mean velocity. It would be very difficult, if not impossible, to reproduce the precise time-dependent inflow conditions for LES that would match Quinn's experiments. Therefore, for simplicity, we apply laminar inflow conditions for all four jets. Figure 2 shows three inflow velocity profiles we use in our simulations. The uniform streamwise velocity shown as Fig. 2(a) is similar to that used in Tsuchiya's experiment.[9] Figures 2(b) and 2(c) represent streamwise and spanwise (also lateral for square jet) velocity profiles which are somewhat similar to the mean velocity profiles used in Quinn's experiment[11] for square jet. An inflow sensitivity study is performed to understand the effect of inflow on the various flow features. The square jet is chosen for this exercise as the computational and experimental inflow profiles are most dissimilar in this case.

C. Side boundary conditions

In the experiments listed in Table I, the flow field is either semi-infinite as claimed in Tsuchiya's experiment[9] or

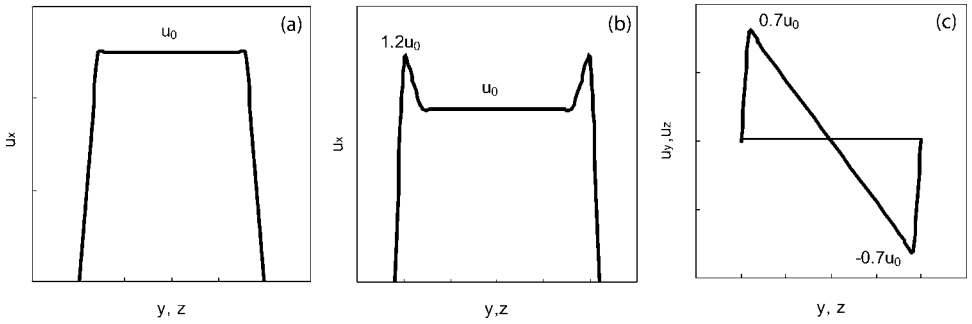

FIG. 2. Laminar inflow velocity profiles. (a) and (b) Streamwise velocity profiles; (c) spanwise and lateral velocity profiles.

in a very large chamber, e.g., $W/w=H/h=610$, as in Quinn's[11] setup. In general, it is not practical to employ such a large flow field for a numerical simulation due to the extremely high computational cost. In this work, we try both periodic boundary and "at rest" boundary conditions. Computationally, the former is easier to implement. In the implementation of the at rest boundary condition along the spanwise and lateral directions, we simply specify zero velocity and constant density (pressure).

Initially, the velocity field is $\mathbf{u}=0$ everywhere in the computational domain except the jet exit area (at inflow boundary) where $\mathbf{u}=\mathbf{u}_b$. The initial density field is uniform at ρ_0. We assume $\rho_b=\rho_0$ at the jet exit. After an initial run of $1000T_0$ ($T_0=\mathrm{De}/u_0$), the streamwise velocity and the square of streamwise velocity are averaged over time for another $1000T_0$ to obtain the MSV $u(x,y,z)$ and streamwise turbulence intensity $u'(x,y,z)$.

III. LATTICE BOLTZMANN METHOD FOR LES OF TURBULENCE

Instead of solving the usual continuum hydrodynamic equations, i.e., NS equations, LBE deals with the evolution of discretized single-particle velocity distribution functions in time and space. The ensuing lattice-based equation conserves mass, momentum, and energy. The local macroscopic quantities such as density and momentum are computed from the moments of these distribution functions.[30] Pressure is obtained from the state equation of isothermal ideal gas $p=c_s^2\rho$.[35] Numerical implementation of LBE is simple and straightforward. In general, it consists of two computational substeps: relaxation (collision) and advection (streaming).

This paper is a part of our continuing effort to adapt and assess LBM for DNS and LES of turbulence. It has been found that the SRT-LBE model performs quite well for high-resolution DNS and LES of decaying isotopic turbulence.[34,44] In these studies, it was determined that the Smagorinsky coefficient (C_s) value of 0.1 captured the spectral behavior and kinetic energy decay most accurately. The physical reasons underlying the reduction of C_s from NS-LES value of 0.17 are also given. In Ref. 45 it is clearly established that SRT-LBE performs well in DNS of homogeneous shear flow. Despite the success of the SRT-LBE model in DNS and decaying turbulence LES, it has been speculated that the more complex MRT-LBE may be necessary for LES of forced turbulence at relatively high Reynolds numbers. Towards this end, we develop an efficient implementation of the MRT-LBE scheme for LES application in Ref. 41. In this section, we compare some SRT and MRT results for RTJ to clearly establish the suitability of the two schemes.

We begin by providing brief introductions to the two LBE schemes in the context of the D3Q19 lattice model. In this lattice model, the 3D discrete phase space is defined by a cubic lattice with 19 discrete particle velocities $\{\mathbf{e}_\alpha|\alpha=0,1,\ldots,18\}$ as

$$\mathbf{e}_\alpha=\begin{cases}(0,0,0) & \alpha=0,\\ (\pm1,0,0),(0,\pm1,0),(0,0,\pm1) & \alpha=1\text{–}6,\\ (\pm1,\pm1,0),(\pm1,0,\pm1),(0,\pm1,\pm1) & \alpha=7\text{–}18.\end{cases}$$

SRT-LBE model. In SRT, the collision operator only involves a single relaxation time τ through BGK approximation[46] so that all the moments of the distribution functions relax with the same time scale. This relaxation time is determined from the fluid viscosity ν. The ensuing collision operator is easy to implement, leading to widespread use of this model.

The SRT-LBE for LES is given as

$$f_\alpha(\mathbf{r}+\mathbf{e}_\alpha\delta_t,t+\delta_t)=f_\alpha(\mathbf{r},t)-\frac{1}{\tau^*}[f_\alpha(\mathbf{r},t)-f_\alpha^{(\mathrm{eq})}(\mathbf{r},t)], \quad (1)$$

where f_α and $f_\alpha^{(\mathrm{eq})}$, $\alpha=0, 1, \ldots, 18$, represent the 19 distribution functions and their equilibria, respectively, for the resolved scales; δ_t is the discrete time-step size; and τ^* is effective LES relaxation time which will be explained shortly.

The equilibria for incompressible flow are[47]

$$f_\alpha^{(\mathrm{eq})}=w_\alpha\left\{\delta\rho+\rho_0\left[\frac{3\mathbf{e}_\alpha\cdot\mathbf{u}}{c^2}+\frac{9(\mathbf{e}_\alpha\cdot\mathbf{u})^2}{2c^4}-\frac{3u^2}{2c^2}\right]\right\}, \quad (2)$$

where $\delta\rho$ is the density fluctuation, ρ_0 is the constant mean density of the system, and $c=\delta_x/\delta_t$. In LBM the values of ρ_0, δ_t, and δ_x are all typically set to unity. The sound speed in this model is $c_s=c/\sqrt{3}$. The total density is $\rho=\rho_0+\delta\rho$. The weighting factors w_α for the D3Q19 model are $w_0=1/3$, $w_{1\text{–}6}=1/18$, and $w_{7\text{–}18}=1/36$. The mass and momentum conservations are strictly enforced:

$$\delta\rho=\sum_\alpha f_\alpha=\sum_\alpha f_\alpha^{(\mathrm{eq})}, \quad (3a)$$

$$\rho_0\mathbf{u}=\sum_\alpha \mathbf{e}_\alpha f_\alpha=\sum_\alpha \mathbf{e}_\alpha f_\alpha^{(\mathrm{eq})}. \quad (3b)$$

The fluid kinematic viscosity ν has the following relation with the relaxation time τ:

$$\nu=\frac{1}{3}\left(\tau-\frac{1}{2}\right)c\delta_x, \quad \tau=\frac{3\nu}{c\delta_x}+\frac{1}{2}. \quad (4)$$

To implement the Smagorinsky model,[48,49] the eddy viscosity ν_t is calculated from the filtered strain rate $S_{ij}=(\partial_j u_i+\partial_i u_j)/2$ and a filter length scale δ_x as follows:

$$\nu_t=(C_s\delta_x)^2S, \quad (5a)$$

$$S=\sqrt{\langle S_{ij}S_{ij}\rangle}, \quad (5b)$$

where S is the characteristic filtered strain rate and C_s is the Smagorinsky constant. In all our simulations, we use $C_s=0.1$.[34] With C_s and δ_x given, τ_t can be obtained[50]

$$\tau_t=\frac{1}{2}(\sqrt{\tau^2+18\sqrt{2}(\rho_0c^2)^{-1}C_s^2\delta_x S}-\tau). \quad (6)$$

The LES effective viscosity ν^* and relaxation time τ^* are

$$\nu^*=\nu+\nu_t=\frac{1}{3}\left(\tau^*-\frac{1}{2}\right)c\delta_x, \quad \tau^*=\tau+\tau_t. \quad (7)$$

In SRT, S_{ij} can be obtained directly from the second moment of the nonequilibrium distribution functions, rather than resorting to finite difference estimations. This leads to improved accuracy and stability over finite difference methods.[34] The details of implementation of SRT for LES can be found elsewhere.[34]

One major disadvantage of the SRT collision model is the lack of freedom to quickly dissipate nonphysical small-scale oscillations induced by spurious conserved quantities in the LBM system.[51] These small-scale oscillations may not only lead to numerical instability but also compete with physical turbulence fluctuations in a LES computation and degrade physical accuracy.[41] Thus, all measures must be taken to minimize numerical oscillations.

MRT-LBE model. In general, the MRT-LBE model has the same computational components, relaxation (collision) and advection (streaming), as the SRT-LBE model. The significant difference between these two models is in the collision operator. With the use of multiple relaxation times, MRT-LBE enables different moments to relax at different time rates. Due to this freedom, it is possible to choose appropriate relaxation times to rapidly dissipate nonhydrodynamic moments and suppress nonphysical small-scale oscillations quickly so that better numerical stability[38] and more accurate boundary implementation[40,41] can be achieved. This rapid equilibration of nonhydrodynamic modes does not affect the conservation of the hydrodynamic quantities.

The MRT-LBE is modeled as

$$|f(\mathbf{r}+\mathbf{e}_\alpha\delta_t,t+\delta_t)\rangle - |f(\mathbf{r},t)\rangle = -M^{-1}\hat{S}[|m(\mathbf{r},t)\rangle - |m^{(\mathrm{eq})}\times(\mathbf{r},t)\rangle]. \tag{8}$$

The Dirac notation of ket $|\cdot\rangle$ represents column vector, i.e., $|f(\mathbf{r}+\mathbf{e}_\alpha\delta_t,t+\delta_t)\rangle \equiv [f_0(\mathbf{r}+\mathbf{e}_\alpha\delta_t,t+\delta_t), f_1(\mathbf{r}+\mathbf{e}_\alpha\delta_t, t+\delta_t), \ldots, f_{18}(\mathbf{r}+\mathbf{e}_\alpha\delta_t,t+\delta_t)]^T$. Notations $|m\rangle$ and $|m^{(\mathrm{eq})}\rangle$ are used to represent the 19 moments of $|f\rangle$ and the corresponding equilibria of $|m\rangle$, respectively. The transformation matrix M will be described below. The diagonal collision matrix $\hat{S}$ is defined as

$$\hat{S} \equiv \mathrm{diag}(0,s_1,s_2,0,s_4,0,s_4,0,s_4,s_9,s_2,s_9,s_2,s_9,s_9,s_9,s_{16},s_{16},s_{16}), \tag{9}$$

where the s_i's ($i=1, 2, 4, 9, 16$) are parameters corresponding to various relaxation time scales. In MRT-LBE, particle collision occurs in a moment space spanned by $|m\rangle$, while particle streaming happens in a velocity space spanned by $|f\rangle$. The spaces are related through a linear mapping: $|m\rangle = M|f\rangle$ or $|f\rangle = M^{-1}|m\rangle$. The formulations of $|m^{(\mathrm{eq})}\rangle$ and the values of M and $\hat{S}$ for the D3Q19 lattice model can be found in Ref. 39. The kinematic viscosity ν and the bulk viscosity ζ of this model are

$$\nu = \frac{1}{3}\left(\frac{1}{s_9}-\frac{1}{2}\right)c\delta_x, \tag{10}$$

and

$$\zeta = \frac{2}{9}\left(\frac{1}{s_1}-\frac{1}{2}\right)c\delta_x. \tag{11}$$

In the LES extension, eddy viscosity ν_t is introduced and the effective kinematic viscosity ν^* is then determined by

$$\nu^* = \nu + \nu_t \tag{12}$$

where ν_t is again computed by the Smagorinsky model [Eqs. (5a) and (5b)]. The effective viscosity and s_9^* are related as follows:

$$\nu^* = \frac{1}{3}\left(\frac{1}{s_9^*}-\frac{1}{2}\right)c\delta_x, \quad s_9^* = \frac{2c\delta_x}{6\nu^* + c\delta_x}. \tag{13}$$

For the sake of simplicity without loss of numerical accuracy,[34] here we use the strain rate from the previous time step to compute ν_t in Eqs. (5a) and (5b).

In MRT, the strain-rate tensor can be computed from the nonequilibrium moments directly. The formulas to compute S_{ij} for the D3Q19 lattice are given in Ref. 41. Note that, since LBM is an inherently compressible scheme, $S_{ii} \neq 0$.

MRT vs SRT for LES

It has been shown that MRT has the following potential advantages over SRT:

(1) MRT has better stability characteristics than SRT as the nonhydrodynamic moments are rapidly equilibrated by choosing appropriate relaxation times.[38]
(2) MRT has better accuracy characteristics than SRT. In the event the spurious modes do not destabilize the calculations in SRT, the small-scale oscillations they induce can contaminate the hydrodynamic moments.[41]
(3) Due to the above two reasons, the maximum Reynolds number that can be attained with MRT is typically four times larger than that with SRT on the same grid.[38]

These advantages are particularly crucial for LES of highly unsteady flows. In LES the smallest resolved motions are quite energetic, resulting in rapid magnification of any numerical error. In DNS, the smallest resolved scales contain little energy and therefore numerical error at the grid scale is less disruptive.

We now perform a preliminary comparison between MRT and SRT models for LES. The test case chosen for comparison is jet II of AR=1.5 and Re=25 900.

Figures 3 and 4 show the instantaneous streamwise ve-

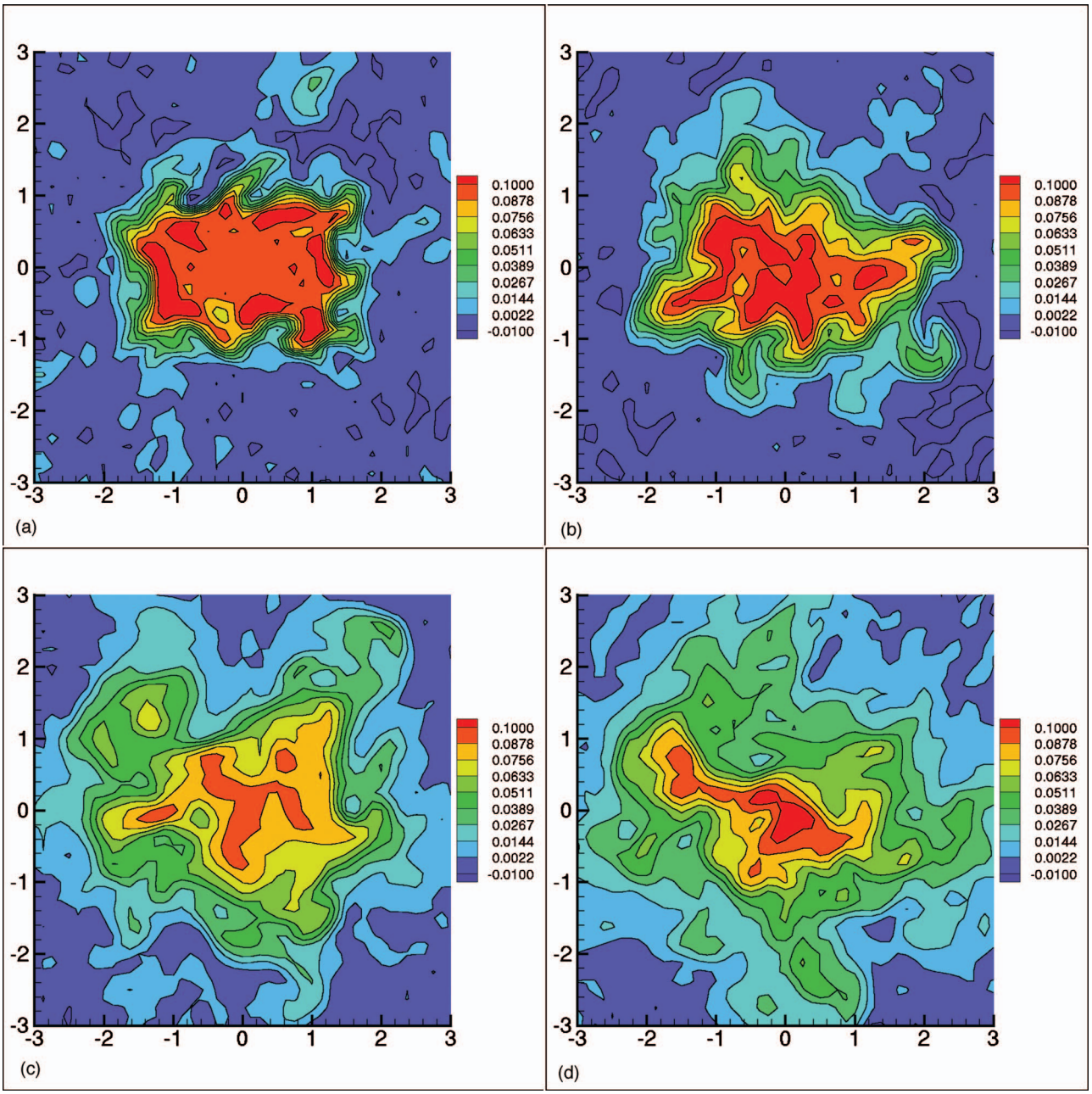

FIG. 3. (Color). Contours of instantaneous streamwise velocity of jet II on *Y-Z* planes at different downstream locations from MRT simulation, $t=0.013$ (s). (a) $x=2h$; (b) $x=4h$; (c) $x=8h$; and (d) $x=10h$.

locity contours at different downstream locations obtained from MRT simulation at two different times. In the figures, only jet core area is plotted. The dense contour spacings close to the jet exit (PC region) indicate high velocity gradients. The sparse spacings of the contours downstream imply gentler velocity gradients as significant mixing has occurred.

Next, we simulate the same flow under identical conditions with SRT. Figure 5 shows the instantaneous streamwise SRT velocity contours at the same time and downstream locations as in Fig. 3. These results appear nonphysical as steep gradients persist well into the characteristic decay region where the potential core should be well mixed. Further, the instantaneous jet structure exhibits symmetries atypical of turbulence. These nonphysical symmetric structures are induced by the symmetric side boundary condition and propagate unattenuated into the core area through the spurious conserved quantities.[51]

The difference between MRT and SRT is quantified in Fig. 6. The streamwise velocity spectra from the two methods at several streamwise locations are shown in the figure. The MRT spectra exhibit good behavior with very little energy in scales of the order of grid size. The SRT spectra, however, indicate considerable energy at the smallest scales. This is due to the numerical oscillations induced by undamped spurious modes. Further comparisons will be presented later.

The evidence presented clearly shows that MRT is better

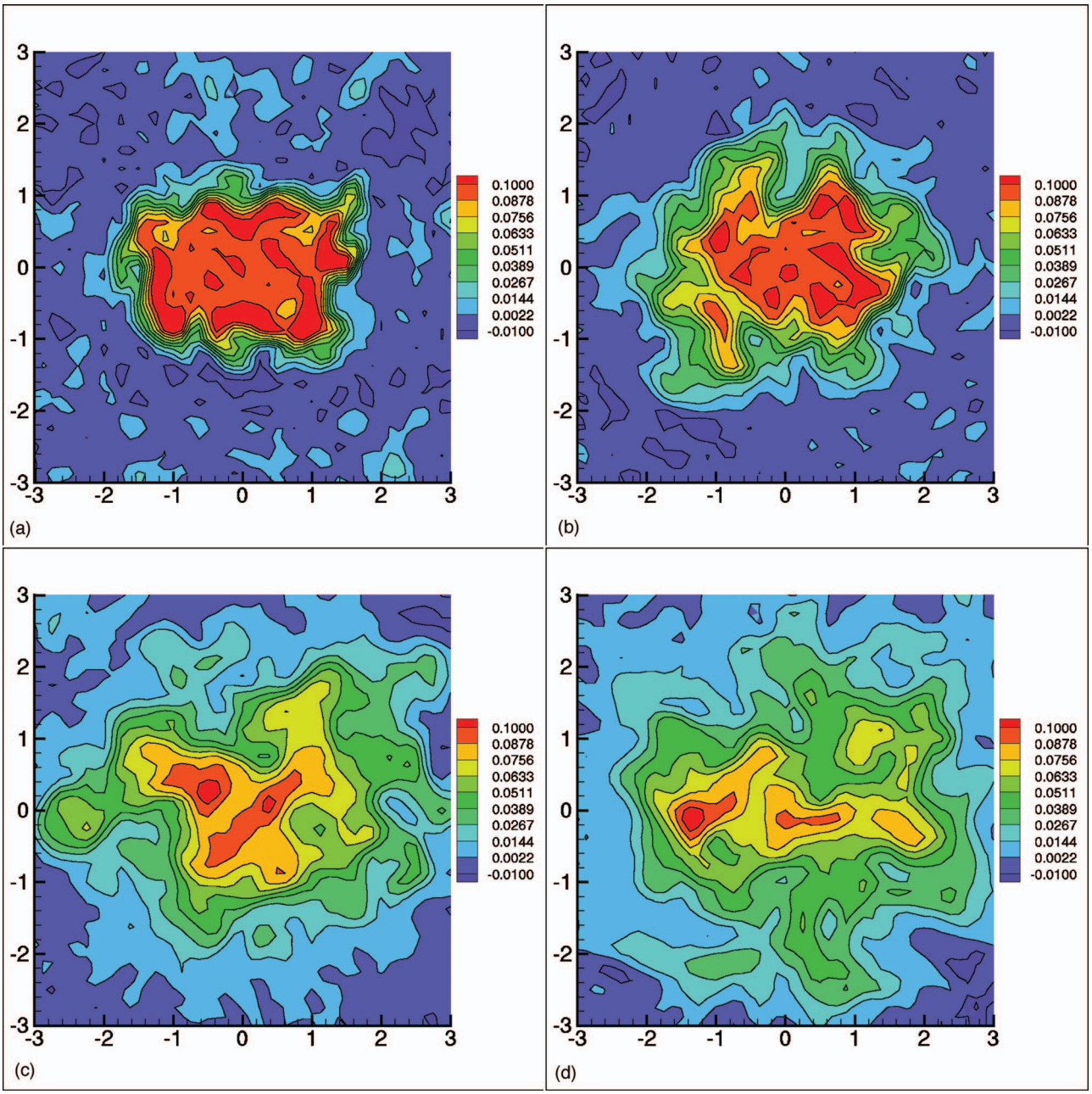

FIG. 4. (Color). Contours of instantaneous streamwise velocity of jet II on *Y-Z* planes at different downstream locations from MRT simulation, $t=0.017$ (s). (a) $x=2h$; (b) $x=4h$; (c) $x=8h$; and (d) $x=10h$.

suited for LES applications. In the remainder of this paper, all computations are performed using the MRT model.

IV. RESULTS AND DISCUSSION

The objective of this work is to simulate the generic aspects of RTJs and not necessarily reproduce the specifics of any particular experiment. To a large extent this is due to the fact that the unsteady turbulent inflow conditions are difficult, if not impossible, to duplicate in the LES computations. It is very important to note that even NS-based methods (RANS,[11] DNS,[43] and LES[25,27]) fail to capture some important near-field aspects of RTJs for this same reason.

We perform simulations and compare our statistical results with data wherever possible in order to validate the capability of the novel LBM-LES approach. The various experimental works present results in terms of different flow parameters and comparisons are made for all possible variables. In what follows, we present our results in two parts: square jet and RTJ computations.

A. Square jet

Computations are performed with three different combinations of inflow and side boundary conditions given in Table III. Of these, case 1 and case 2 have similar streamwise inflow velocity conditions (no spanwise or lateral flow) but different side boundary conditions. In case 3, the inflow

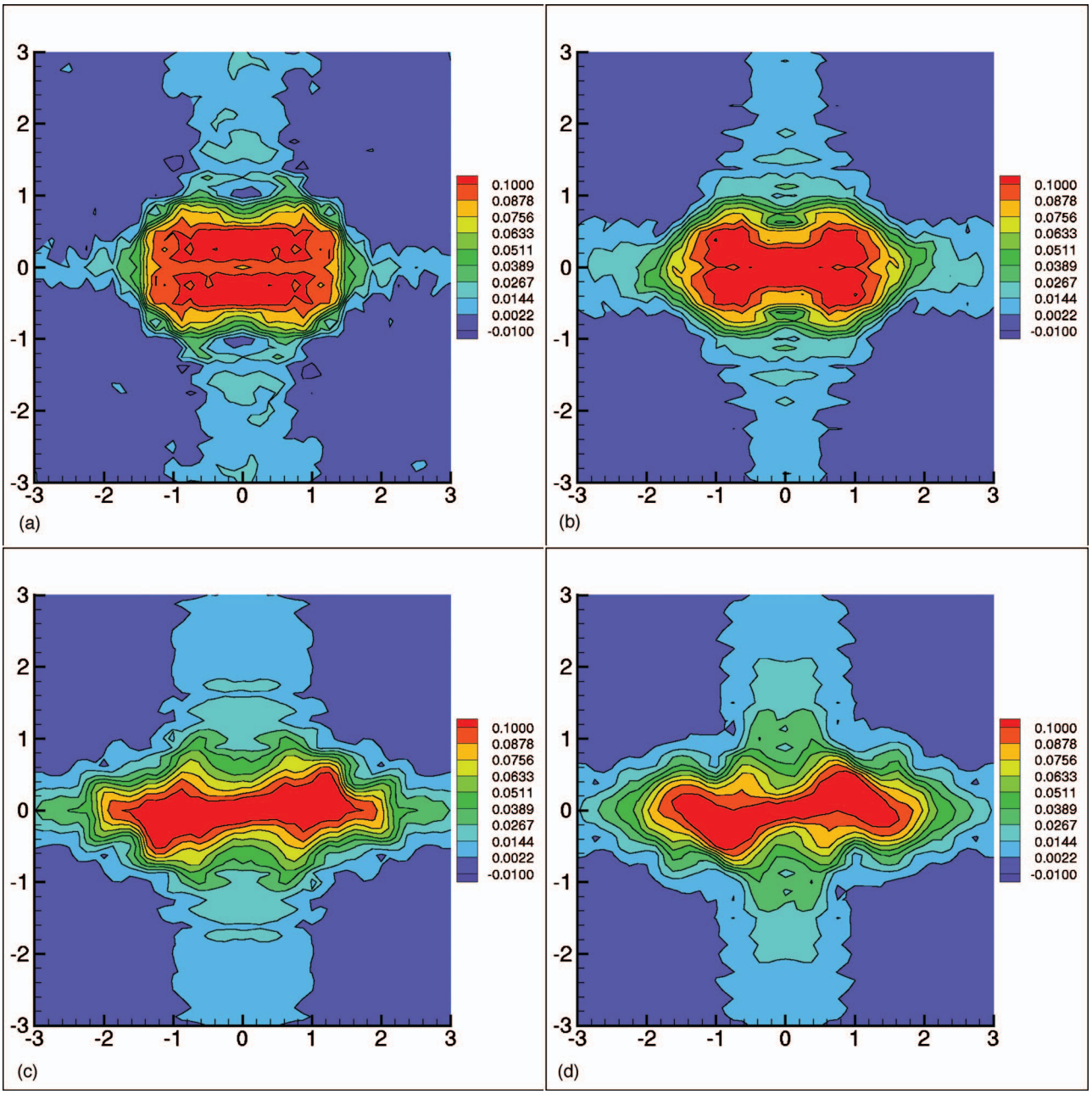

FIG. 5. (Color). Contours of instantaneous streamwise velocity of jet II on *Y-Z* planes at different downstream locations from SRT simulation, $t=0.013$ (s). (a) $x=2h$; (b) $x=4h$; (c) $x=8h$; and (d) $x=10h$.

velocity profiles are somewhat similar to the mean velocity profiles in Quinn's experiment.[11] The most important difference is that the computational inflow is laminar, whereas the experimental inflow[11] is turbulent.

1. Centerline MSV decay

We expect the initial centerline MSV evolution to be strongly dependent on the inflow condition.[11] Figure 7 shows the decay of normalized MSV (u_{cl}/u_{max}) on the jet centerline. Here, u_{max} is the maximum MSV of u_{cl} typically located at *Vena Contracta*. Three lines are LBM computational results and symbols are experimental data of Quinn and Militzer.[11] It must be noted that the Quinn experiment uses nozzle-type jet exit with strong curvature of inflow streamlines leading to a pronounced *Vena Contracta* effect. In LBM simulations, only case 3 is somewhat close to the experimental mean inflow velocity condition. Clearly, case 1 and case 2 yield weak *Vena Contracta* effect but reproduce the experimental measurement adequately well beyond the *Vena Contracta*. Case 3 does capture the *Vena Contracta* effect, but is distinctly different from experimental data at later times. It appears that matching the centerline MSV requires accurate specification of the inflow profile. Unfortunately not enough information is known from the reference[11] to specify the right inflow conditions. It should be pointed out that NS-based calculations of Quinn and Militzer[11] also yield similar degree of disagreement at the near field (Fig. 4 in Ref. 11) as the current computations.

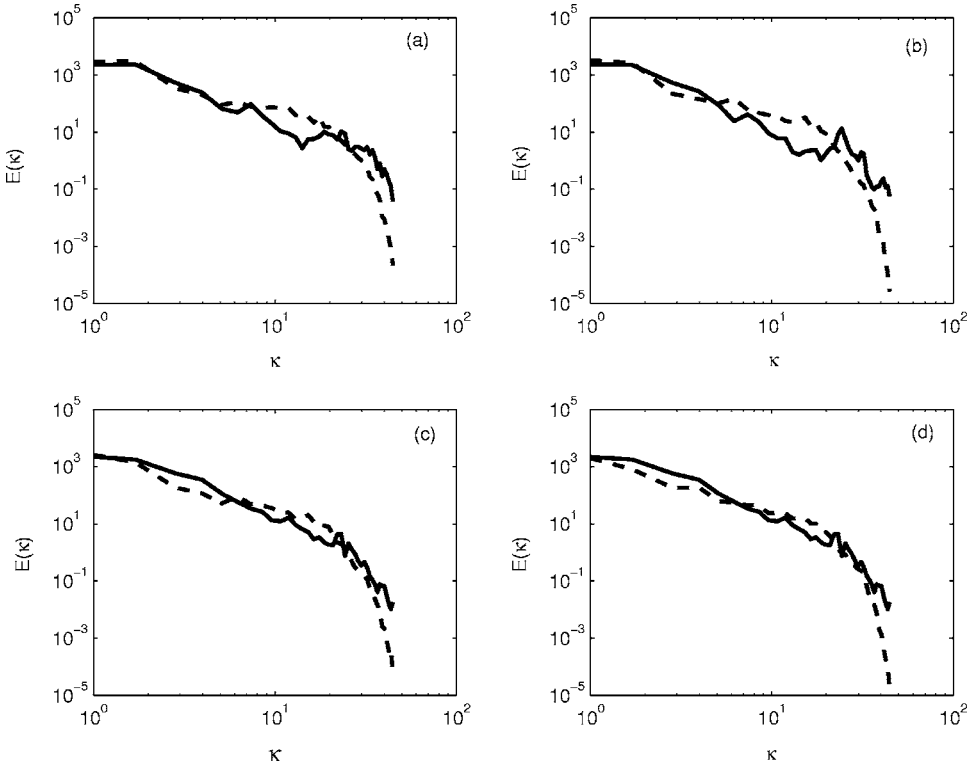

FIG. 6. Streamwise velocity spectra of MRT vs SRT at different downstream locations. — (solid line): SRT; --- (dashed line): MRT. (a) $x=2h$; (b) $x=4h$; (c) $x=8h$; and (d) $x=10h$.

2. MSV profiles

It is known from experiments that MSV profiles (when suitably normalized) exhibit self-similar behavior in the CD region. The self-similar behavior indicates that these profiles are not very sensitive to the unsteadiness in the inflow conditions. Figure 8 shows the MSV profiles along the Y direction at different X locations. Very good agreement between the experiment[11] (symbols) and LBM simulations (lines) is seen at all locations except the location ($x/\mathrm{De}=0.28$), which is very close to the jet exit (PC region). At this location, the MSV profile is again strongly dependent on the inflow velocity condition. As seen in the figure, case 3 of LBM (dashed line) captures the experimental profile the best at this location.

3. Streamwise turbulence intensity

The computed spanwise profiles of streamwise turbulence intensity along the Y direction at various downstream locations are presented along with experimental results in Fig. 9. Although LBM simulations capture the profile shapes at each location, the magnitudes of turbulence intensity are quantitatively different. We speculate that this is due to the lack of turbulent fluctuations in the inflow condition. Because of the absence of turbulent transport and the presence of steep mean gradients, higher levels of turbulence are obtained in the computation. Further, the strong streamwise curvature effect that leads to a pronounced *Vena Contracta* in the experiment also stabilizes the flow reducing turbulence production in the experiment.

It would be the best to compare our results against experiments which also use laminar inflow conditions, e.g., Tsuchiya's experiment for RTJs.[9] Unfortunately, streamwise turbulence intensity profiles for square jet are not available in Tsuchiya's experiment. It will be seen later in jets II and IV,

TABLE III. Jet exit slot velocity profiles and side boundary conditions.

Case number	u_x	u_y, u_z	Side boundary conditions
1	Fig. 2(a)	0	Periodic
2	Fig. 2(b)	0	At rest
3	Fig. 2(b)	Fig. 2(c)	At rest

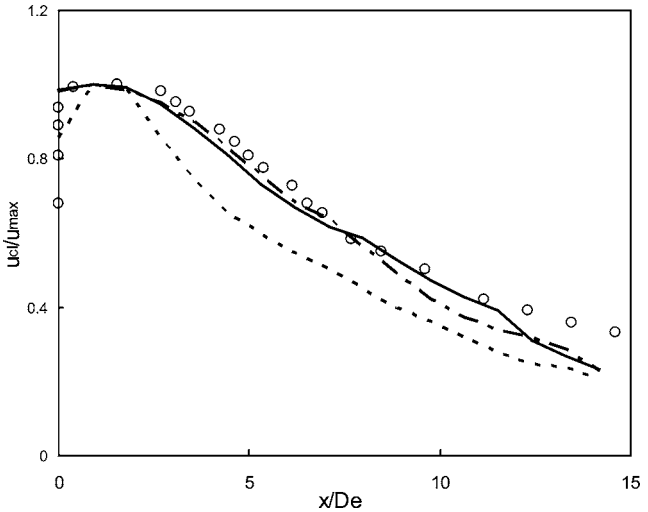

FIG. 7. Near-field normalized MSV development of square jet on jet centerline. ○: Experiment (Ref. 11). Lines: LBM simulations — (solid line): case 1; -.- (dotted-dashed line): case 2; --- (dashed line): case 3.

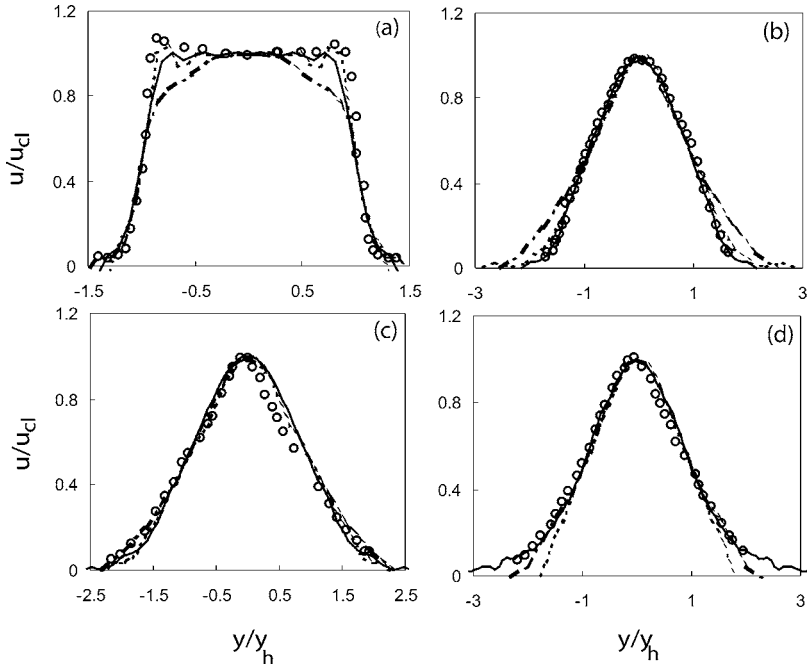

FIG. 8. Normalized MSV profiles of square jet on *Y-Z* planes along *Y* direction at different downstream locations. (a) $x/\mathrm{De}=0.28$; (b) $x/\mathrm{De}=2.658$; (c) $x/\mathrm{De}=4.484$; (d) $x/\mathrm{De}=7.088$. ○: Experiment (Ref. 11). Lines: LBM simulations — (solid line): case 1; -.- (dotted-dashed line): case 2; --- (dashed line): case 3.

where the experimental inflow is laminar, that the agreement is much improved. These results again underscore the importance of unsteady inflow conditions and the need to characterize and quantify inflow conditions in experiments.

The conclusions from the inflow sensitivity study can be summarized as follows. Case 3 does well very close to the jet exit but poorly elsewhere. The good agreement in the immediate proximity of the jet exit slot could, perhaps, be attributed to the fact that the computational laminar inflow profile is similar to the experimental mean turbulent profile. Cases 1 and 2 perform well everywhere except the immediate vicinity of the jet exit. Thus, combinations 2 and 3 yield good agreement with flow physics over a wider portion of the computational domain. The results also indicate that the near-field jet statistical behavior is more sensitive to inflow velocity but less sensitive to the side boundary condition. Therefore, in what follows, we apply the uniform inflow velocity profile [Fig. 2(a)] along with periodic boundary conditions for all RTJ simulations.

B. Rectangular jets

Our objective is to demonstrate that LES can capture the salient physics of RTJs. We reiterate that when the computational and experimental inflow conditions are not identical, the comparisons cannot be expected to be very precise.

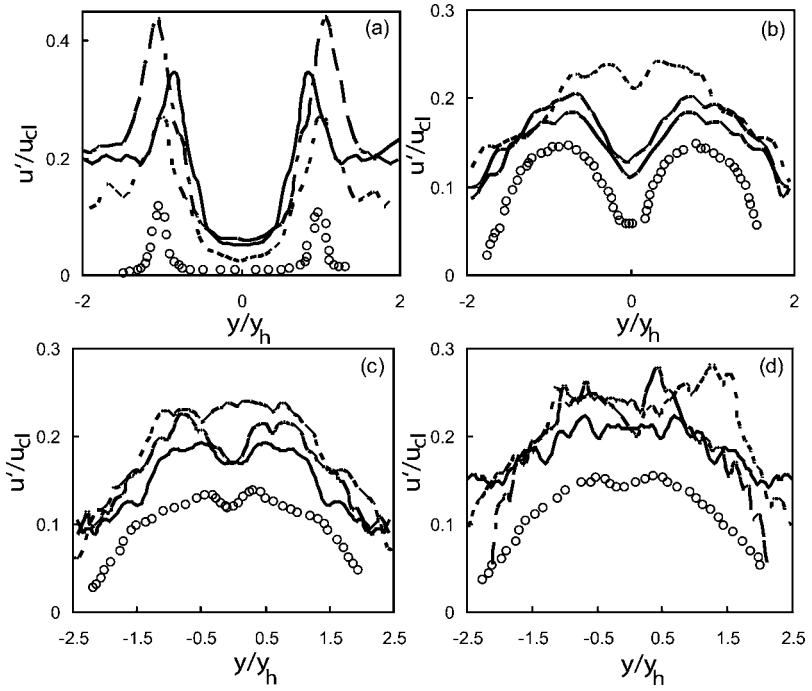

FIG. 9. Spanwise profiles of normalized streamwise turbulence intensity of square jet on *Y-Z* planes along *Y* direction at different downstream locations. (a) $x/\mathrm{De}=0.28$; (b) $x/\mathrm{De}=2.658$; (c) $x/\mathrm{De}=4.484$; and $x/\mathrm{De}=7.088$. ○: Experiment (Ref. 11). Lines: LBM simulations — (solid line): case 1; -.- (dotted-dashed line): case 2; --- (dashed line): case 3.

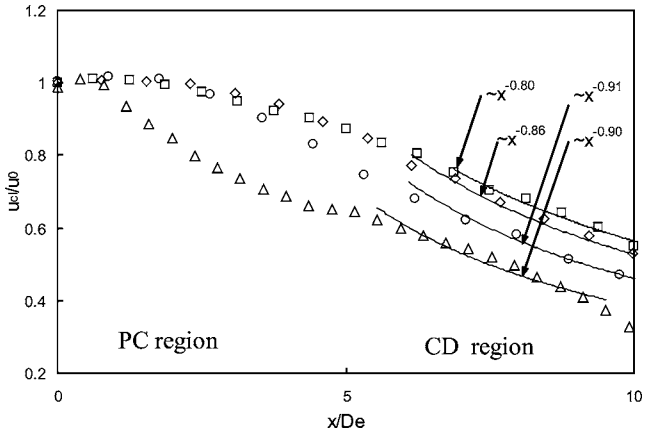

FIG. 10. Decay of the MSV along jet centerline. The decay exponent $n \simeq 1$ in CD region. ○: Jet I; ◇: jet II; □: jet III; △: jet IV.

1. Near-field turbulent mixing

a. Streamwise centerline velocity decay. The MSV decay along the jet centerline of all four jets is shown in Fig. 10. In spite of the fact that uniform inflow velocity profile imposed at the jet exit, weak *Vena Contracta* effect is evident in all cases as the centerline MSV increases slightly near the jet exit. Beyond the *Vena Contracta*, the MSV decreases monotonically. The two near-field subregions PC and CD are identified in the figure. In the CD region, the decay exponents of all cases are around −1, which agrees qualitatively with experimental measurements. The figure demonstrates that the mixing increases, implying penetration decreases, as the jet AR increases. Thus, in larger AR jets, the ambient fluid is entrained into the core more rapidly. The inverse MSV evolution along the jet centerline for jet III is shown in Fig. 11. It can be seen that LBM simulation replicates the decay features reasonably well.

b. Spanwise and lateral profiles of MSV. The spanwise and lateral profiles of MSV at various downstream locations of jets III and IV are presented in Figs. 12 and 13. The velocity profiles in the spanwise and lateral directions exhibit similarity for jet III (Fig. 12) since the AR (=2) is not large enough. For AR=5 (jet IV), the behavior in the two directions is dissimilar (Fig. 13). This phenomenon is well captured by the computed results. The most striking feature is the pronounced saddle-back shape in the spanwise velocity profile at $x=2.8$De [Fig. 13(b)]. Although LBM does not capture the distinct saddle shape, the gentle depression at the center of the computed jet shows that this phenomenon is present in the simulations. This aspect will be further examined later.

c. Jet spread. The jet spread rates in the X-Y and X-Z planes for jets II and III are shown in Figs. 14 and 15, respectively. The spread rates are quantified in terms of lateral half-width (y_h) and spanwise half-width (z_h). Experiments indicate that while y_h increases monotonically, z_h stays nearly constant (even decreases) at early stages and then grows in both directions. The LBM results capture this spread feature adequately well. It is seen that jet II yields better agreement with the corresponding experiment in Fig. 14 than jet III in Fig. 15. This is again due to the fact that the experimental and computational inflow velocity profiles are closer in the case of jet II than jet III. For comparison, SRT-LBE simulation results (dashed line) with identical conditions to MRT-LBE case are plotted in Fig. 14 for jet II. Again, it is clearly seen that MRT-LBE simulation yields much better agreement with the experimental data than SRT-LBE simulation. The difference in the growth rates of y_h and z_h leads to the interesting phenomenon of axis switching in low AR jets.

d. Axis-switching phenomenon. Axis switching refers to the change in the orientation of the major axis of the jet from initial spanwise to lateral direction. This phenomenon is of interest both from fundamental physics and practical application points of view. This behavior is most noticeable in low AR RTJ flows.[4,5,9,14] In Fig. 16, the computed half velocity ($u/u_{cl}=0.5$) contours of jet II on Y-Z planes (right plot) are directly compared with experimental contours (left plot) at approximately the same X locations. The LBM simulation mimics the deformation of the jet spread from the initial rectangular shape with major axis along spanwise ($x=0.06h$) through a rhombuslike shape at a short distance from the exit ($x=4h$) to an ellipse with major axis along the lateral direction ($x=10h$).

The MSV contour lines in Fig. 17 provide more details about the jet deformation. The plots show contour lines of various u/u_{cl} levels in Figs. 17(a) (lateral direction) and 17(b) (spanwise direction). All contour levels larger than $u/u_{cl}=0.3$ first show a tendency to narrow down in the X-Z plane. The higher level contours converge more rapidly than lower level contours. The contours of $u/u_{cl}<0.3$ do not change much initially in the X-Z plane. Beyond $x=6h$ all the contours diverge in the X-Z plane. Meanwhile, in the

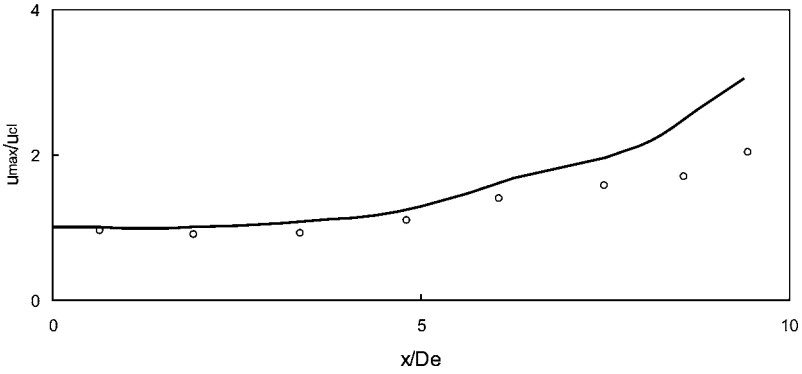

FIG. 11. Near-field inverse MSV decay of jet III along the jet centerline. —: LBM simulation; ○: experiment (Ref. 12).

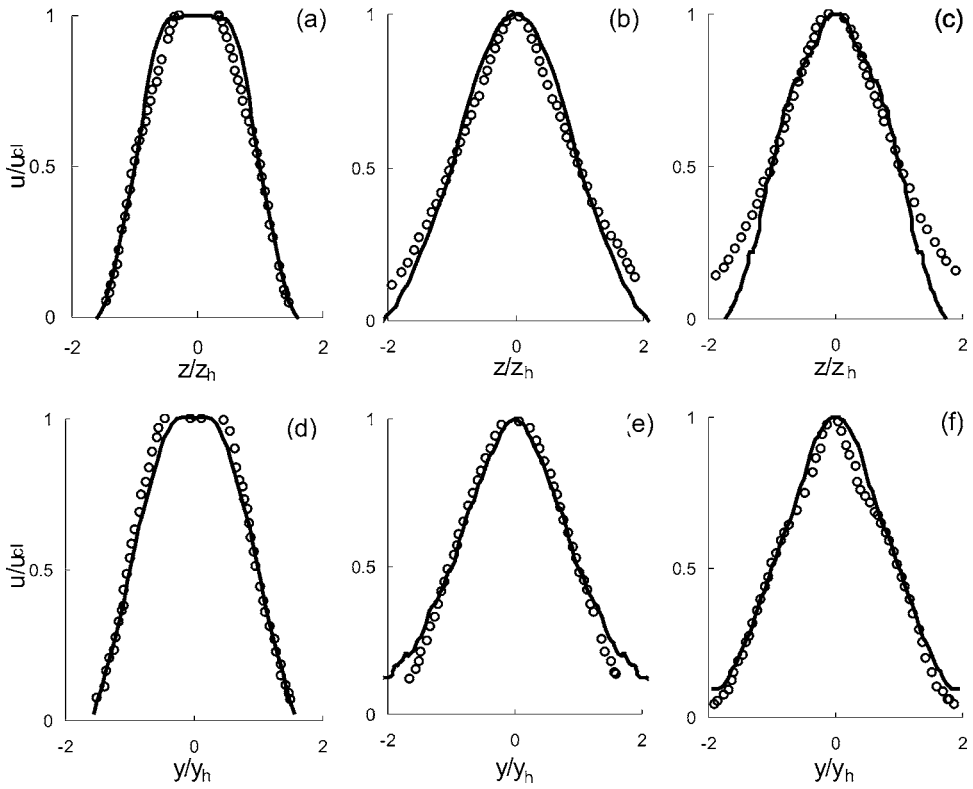

FIG. 12. MSV profiles of jet III in spanwise [(a), (b), and (c)] and lateral direction [(d), (e), and (f)] at different downstream locations along with experimental results. (a) and (d) $x/\mathrm{De}=2$; (b) and (e) $x/\mathrm{De}=5$; (c) and (f) $x/\mathrm{De}=10$. —: LBM simulation; ○: experiment (Ref. 12).

X-Y plane all contours diverge at all times. The lower level contours diverge more rapidly than the higher level ones. Beyond $x=6h$, the divergence rates slow down. Thus, axis switching happens with all contour levels in the proximity of $x=6h$. The divergence/convergence features of the various contour levels provide a quantitative measure of the entrainment characteristics of the jet. For AR=2, the axis-switching behavior is slightly different. Figures 18(a)–18(d) show the MSV contour maps of jet III at different downstream locations. At location $x=0.03\mathrm{De}$ [Fig. 18(a)], the MSV contours are rectangular. The contours are a little more rounded at $x=0.625\mathrm{De}$. The initial close spacing of the contours implies high MSV gradients. At the intermediate streamwise station [Fig. 18(c)], the contours take on an oval shape with wider

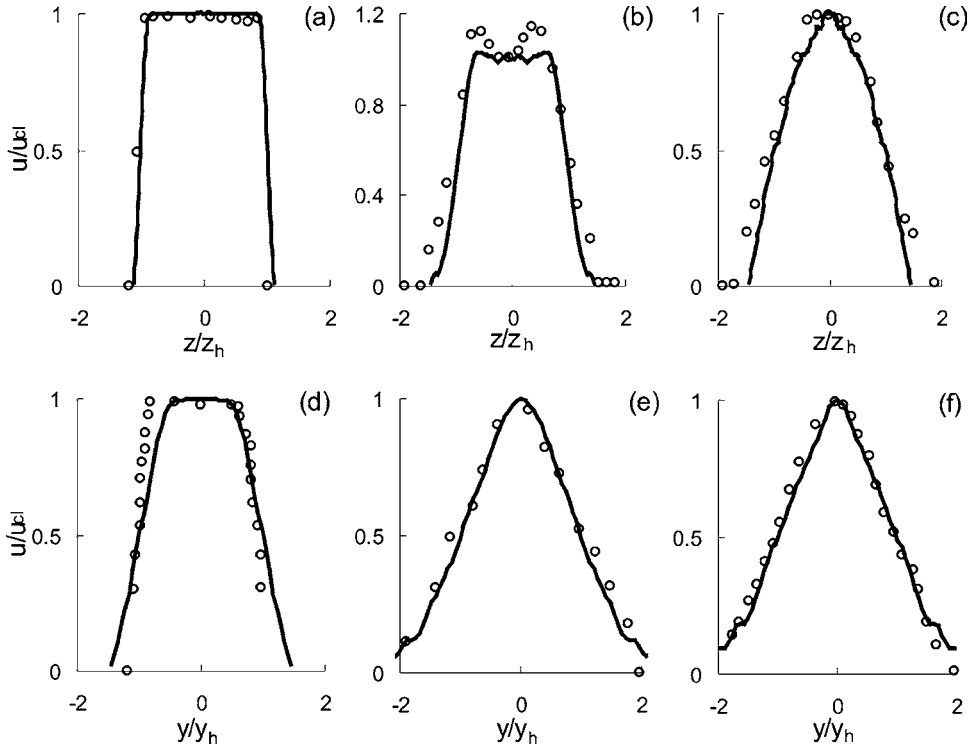

FIG. 13. MSV profiles of jet IV in spanwise [(a), (b), and (c)] and lateral direction [(d), (e), and (f)] at different downstream locations along with experimental results. Spanwise profiles: (a) and (d) $x/\mathrm{De}=0.4$; (b) and (e) $x/\mathrm{De}=2.8$; (c) and (f) $x/\mathrm{De}=5.2$. —: LBM simulation; ○: experiment (Ref. 9).

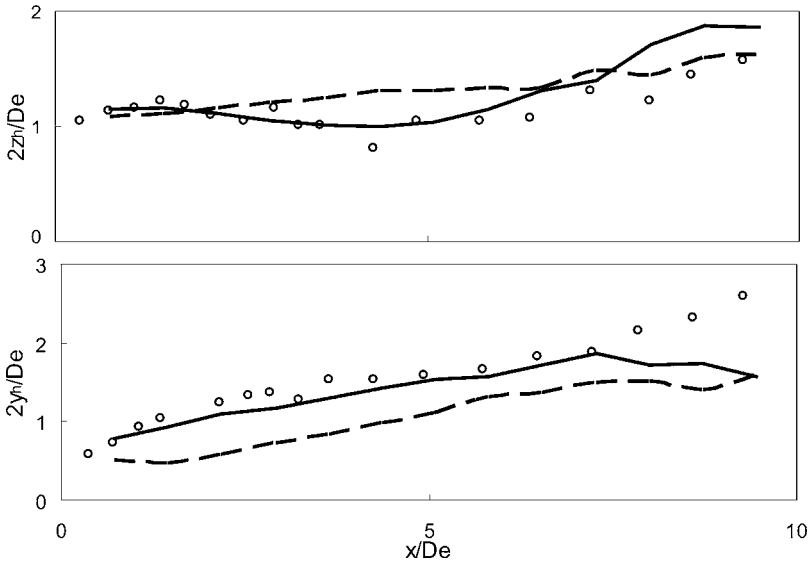

FIG. 14. Half-velocity width development of jet II. Solid lines: MRT-LBE simulation; ---: SRT-LBE simulation; ○: experiment (Ref. 9).

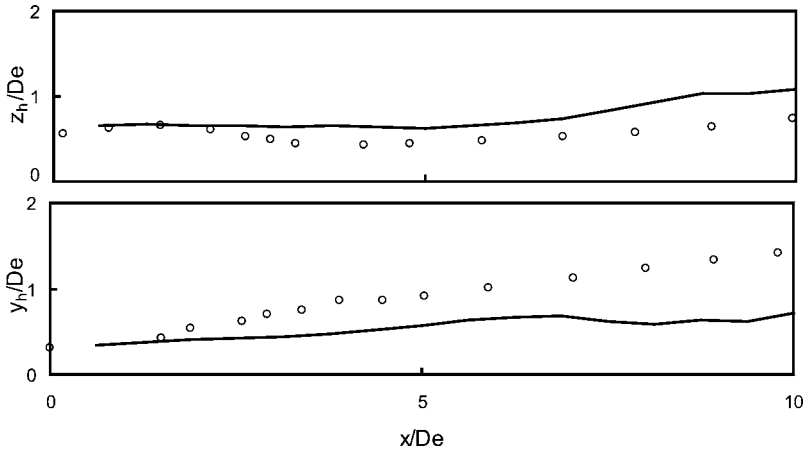

FIG. 15. Half-velocity width development of jet III. —: LBM simulation; ○: experiment (Ref. 13).

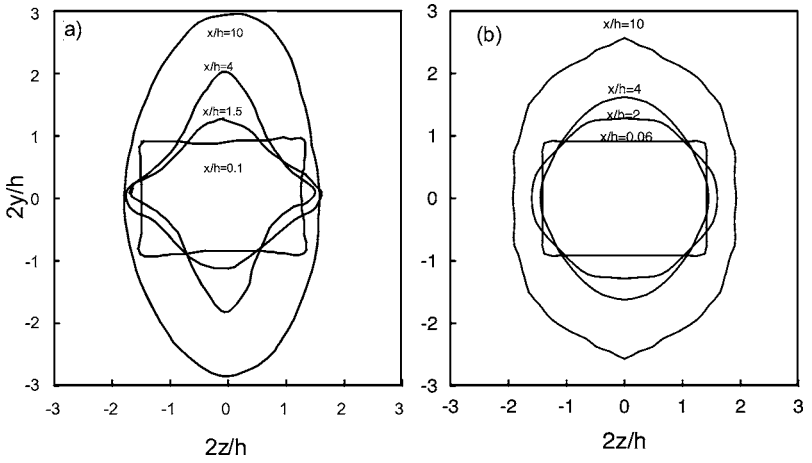

FIG. 16. Half-velocity contour of MSV (u/u_{cl}=0.5) of jet II on *Y*-*Z* planes at different locations; *h* is the jet height. (a) Experiment (Ref. 9); (b) LBM simulation.

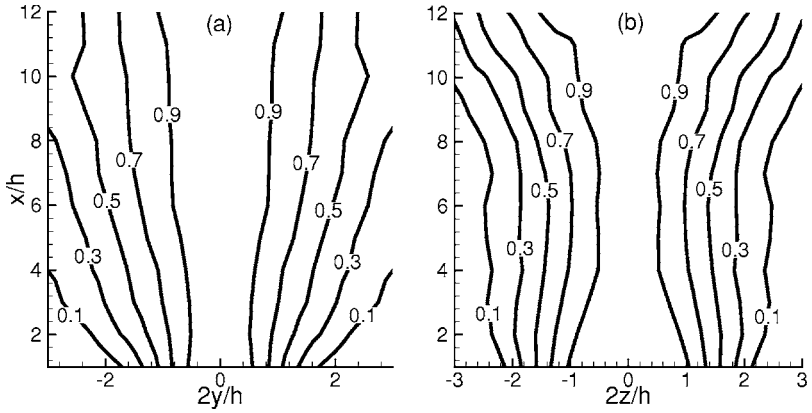

FIG. 17. Contour lines of normalized MSV (u/u_{cl}) of jet II on *X-Y* (a) and *X-Z* (b) planes.

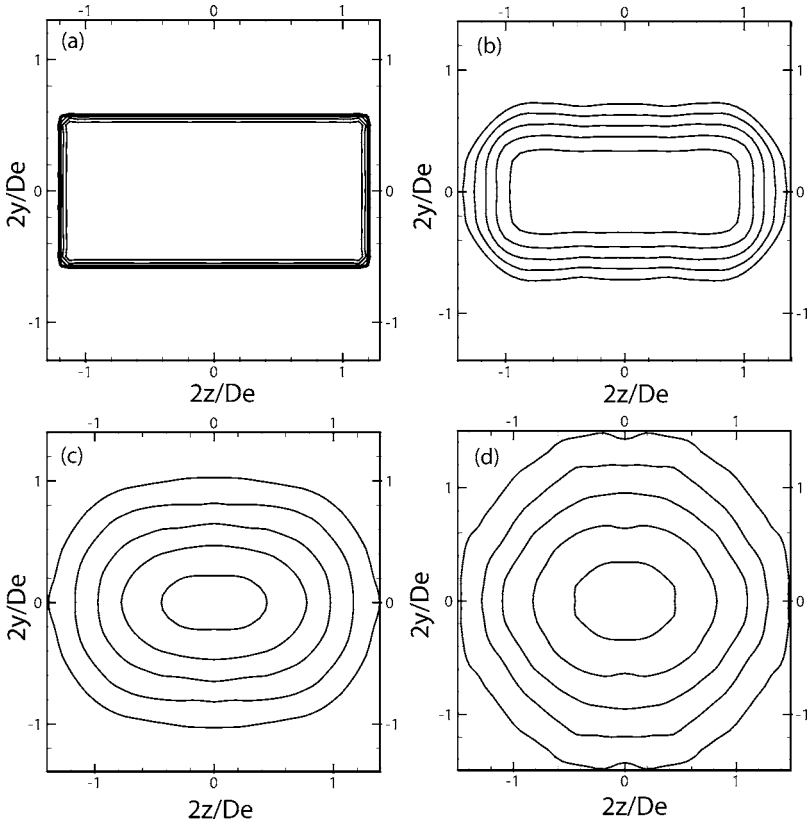

FIG. 18. Normalized MSV (u/u_{cl}) contour development of jet III. The contour levels are 0.45, 0.575, 0.7, 0.825, and 0.9 from jet center outwards. (a) $x/\mathrm{De}=0.03$ (sharp rectangle); (b) $x/\mathrm{De}=0.625$ (rounded rectangle); (c) $x/\mathrm{De}=3.75$ (oval); and (d) $x/\mathrm{De}=6.25$ (circle).

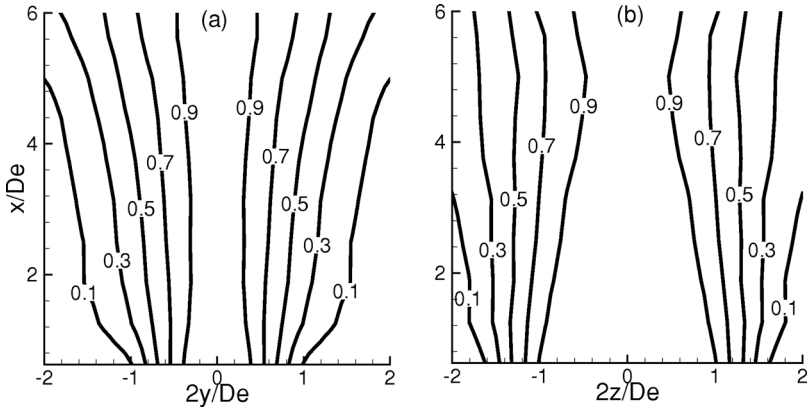

FIG. 19. Contour lines of normalized MSV (u/u_{cl}) of jet III on *X-Y* (a) and *X-Z* (b) planes.

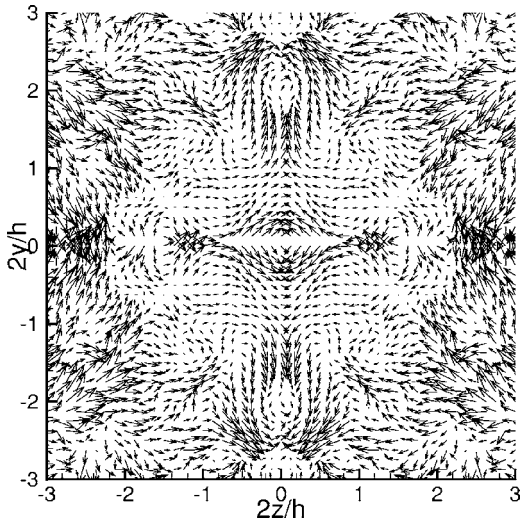

FIG. 20. Velocity vector field of jet II on the *Y-Z* plane at $x=6h$.

spacing implying significant mixing has occurred. From location $x=6.25$ De [Fig. 18(d)] onwards, the contours are essentially circular. The change in shape of the MSV field from rectangular to oval to circular is a characteristic feature of RTJ flow with larger AR. In Quinn's experiments,[15] this rectangular-oval-circular transition for AR=2 has been clearly observed. Figure 19 shows this transition for other contour levels. The details of the entrainment and mixing characteristics of this jet can be inferred from Fig. 19. The contours in Figs. 17 and 19 highlight the basic differences in the mixing features between different AR jets.

e. Physical mechanism of axis switching. According to Ref. 1, axis switching results from interaction between azimuthal velocity and streamwise vorticity. Here, we will try to explain the phenomenon in terms of secondary flow. The mean cross-stream velocity vectors at a representative *X-Y* plane are shown in Fig. 20. At this stage, during the peak of axis switching, the secondary flow comes into the jet core along the spanwise (initial major axis) direction and exits along the lateral (initial minor axis) direction. Molecular and eddy viscosity, on the other hand, attempt to diffuse the momentum out in both directions. Along the spanwise direction, diffusion and secondary flow nearly negate one another, whereas in the lateral direction the two effects augment each other. This results in the half-width growing slowly (or even shrinking) along the spanwise direction and growing more rapidly along the lateral direction leading to axis switching. Motivated by this, further investigation of this phenomenon in a laminar rectangular jet (AR=1.5) is performed in Yu and Girimaji.[52] It is established that the axis-switching phenomenon occurs in laminar jets also. This same mechanism appears to be responsible for axis switching in laminar jets as well.

f. Saddle-back phenomenon. Saddle-back shape of the mean streamwise velocity (MSV) profile in the spanwise (major axis) direction in the CD region is another unique flow feature of RTJ. Saddle-back profiles have long been observed on the spanwise axis of large AR jets, AR$\geqslant$10, in experiments.[4–8,12–14,17] There are few observations of such profiles in RTJs of smaller AR.[4,9] Marsters and Fotheringham[4] and Tsuchiya[9] report saddle-back velocity profiles for smaller values of AR (6.44 and 5) as well. However, such saddle-shaped MSV profile is not evident in the experiment of Quinn[13] in which AR=5. There is still no consensus on the formation mechanism of this kind of veloc-

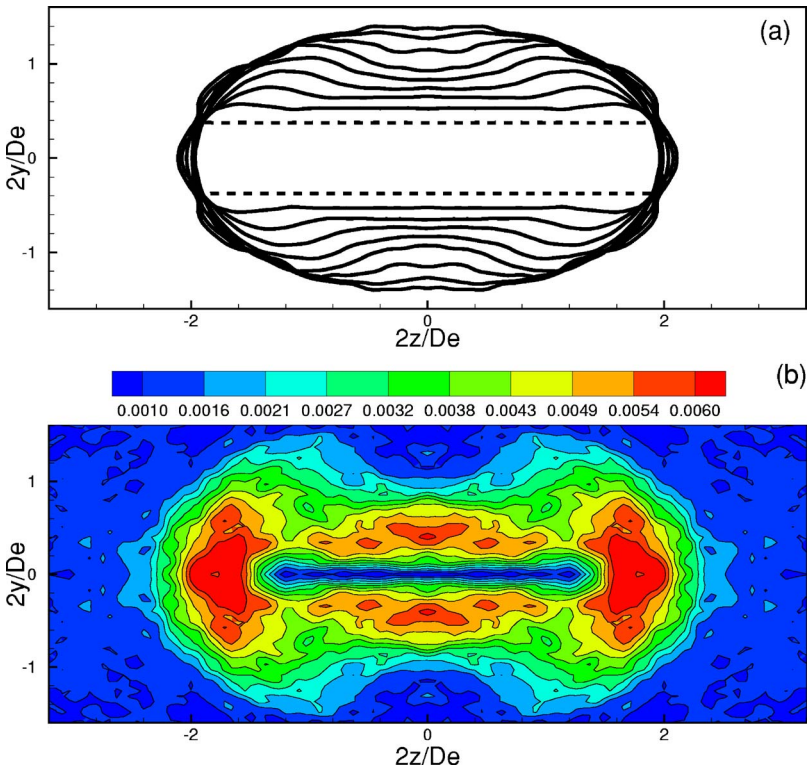

FIG. 21. Near-field flow contours of jet IV on *Y-Z* planes. (a) Normalized MSV ($u/u_{cl}=0.3$) contour lines at different *X* locations: 0.4De, 1.2De, 2.0De, 2.4De, and 3.2De from jet exit (dashed line) outwards; (b) MSV gradient contour at $x=2.0$De.

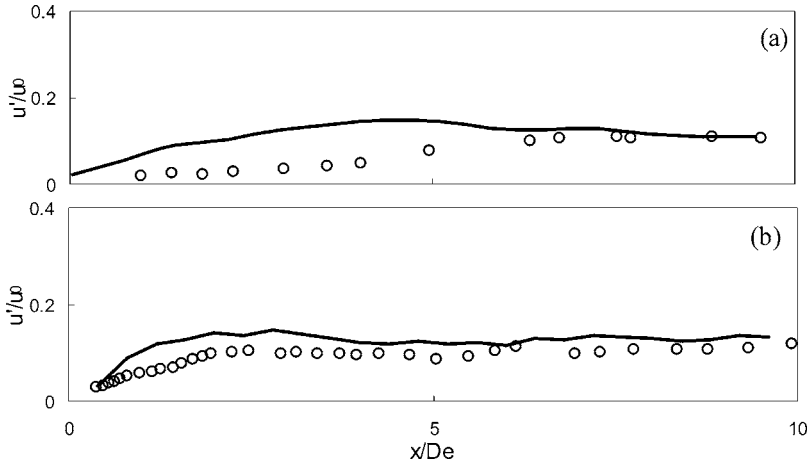

FIG. 22. Turbulence intensity variation along jet centerline. (a) Jet II. (b) Jet IV. —: LBM simulation; ○: experiment (Ref. 9).

ity distribution.[9,18] In our simulations, no distinct saddle-back was observed in the mean velocity profile in the AR =5 jet.

The saddle-back shape [Fig. 12(b)] indicates very rapid mixing in the proximity of $z=0$ plane than at other z planes. We now examine if this rapid mixing is seen in our computations. In Fig. 21(a), the spatial evolution of $u/u_{cl}=0.3$ contour is plotted. The contour goes from the initial rectangle to flattened ellipse to dumbbell shape and ultimately tends to a circle. The dumbbell shape clearly indicates rapid mixing along $z=0$ plane, a forerunner of the saddle-back phenomenon. At larger AR, we expect this localized mixing to intensify leading to a full-fledged saddle-back profile along the centerline.

g. Physical mechanism of saddle-back phenomenon. Tsuchiya[9] suggests that the occurrence of saddle-back profiles might be due to a region where the mixing on the spanwise axis is retarded in comparison with that of the lateral axis. To verify this explanation, we plot velocity gradient magnitude $[\sqrt{(\partial u/\partial y)^2+(\partial u/\partial z)^2}]$ contours at a representative streamwise location ($x=2.0$De) in Fig. 21(b). The steepest gradients are seen at the spanwise edges, indicating the potential for rapid mixing at this location. Along the lateral edges of the jet, the gradients are generally less intense except in the proximity of $z=0$. The strong gradients at this location cause intense local mixing, leading the isocontours to take the observed dumbbell shape. Tsuchiya's explanation is not entirely accurate as the lateral mixing is not more intense than spanwise mixing. The more precise explanation is that the locally intense mixing at $z=0$ leads to the dumbbell shape, even though the mixing rate along the lateral direction is, in general, less than along spanwise directions. Thus, the physical phenomenon that ultimately leads to the saddle shape is captured by our simulations.

h. Centerline turbulence intensity. The streamwise turbulence intensity (u'/u_0) of jets II and IV along the jet centerline is shown in Fig. 22. Corresponding experimental results[9] are also presented. As we can see, in both jets u' increases rapidly near the jet exit where large local shear leads to high values of turbulence production. The experimental results show slower increase of turbulence intensity near the jet exit. In all likelihood, this is due to the fact that the flow transitions to turbulence immediately in the computation and more slowly in the experiment. The agreement is quite good at the later stages. It is noted that the level of agreement is much improved over the square jet case as the experimental and computational inflow conditions are more similar here.

V. CONCLUSION

We perform LES of the near-field features of rectangular turbulent jets using the novel MRT-LBE computational tool. The jets simulated are of low aspect ratios ($AR \leqslant 5$) and of moderately high Reynolds numbers (ranging from 14 000 to 184 000). Computed flow behavior includes centerline MSV decay, jet spread in both spanwise and lateral directions, and streamwise turbulence intensity. The well-known phenomena of RTJ flows, saddle-back velocity profile and axis-switching, are also investigated.

Our findings are now summarized.

(1) The advantages of MRT over SRT for LES computation are clearly established quantitatively and qualitatively.
(2) In the matter of centerline MSV decay and turbulence levels, the degree of agreement between computed results and existing experimental data is not very good. We attribute the lack of close agreement to the fact that these quantities are very sensitive to the unsteady inflow conditions which are not accounted for in our computations. It must be pointed out that this level of disagreement is seen in NS-based calculations as well (RANS of Quinn and Militzer,[11] DNS/LES of Wilson and Demuren,[25] DNS of Chyczewski *et al.*,[43] and LES of Feiz *et al.*[27]).
(3) With regard to normalized MSV profiles, the agreement between computations and experiments is good. It has been known that these self-similar profiles are quite insensitive to the inflow conditions.
(4) The axis-switching phenomenon is well captured by the computations. The underlying flow physics is investigated and explained. The saddle-back feature is not as distinct in the computation as in the experiment.

However, we do identify the physics that subsequently leads to saddle-back profile.

While some elements of LBM applications to LES require future investigation, the overall indications are encouraging.

ACKNOWLEDGMENT

This work was supported by the United States Air Force Office for Scientific Research (AFOSR) under Grant No. F49620-01-1-0142.

[1] E. J. Gutmark and F. F. Grinstein, "Flow control with noncircular jets," Annu. Rev. Fluid Mech. **31**, 239 (1999).
[2] P. M. Sforza, M. H. Steiger, and N. Trentacoste, "Studies on three dimensional viscous jets," AIAA J. **4**, 800 (1966).
[3] P. M. Sforza, "A quasi-axisymmetric approximation for turbulent three-dimensional jets and weaks," AIAA J. **7**, 1380 (1969).
[4] G. F. Marsters and J. Fotheringham, "The influence of aspect ratio on incompressible, turbulent flows from rectangular slots," Aeronaut. Q. **31**, 285 (1980).
[5] G. F. Marsters, "Spanwise velocity distributions in jets from rectangular slots," AIAA J. **19**, 148 (1981).
[6] A. A. Sfeir, "The velocity and temperature fields of rectangular jets," Int. J. Heat Mass Transfer **19**, 1289 (1976).
[7] A. A. Sfeir, "Investigation of three-dimensional turbulent rectangular jets," AIAA J. **17**, 1055 (1979).
[8] N. Trentacoste and P. M. Sforza, "Further experimental results for three-dimensional free jets," AIAA J. **5**, 885 (1967).
[9] Y. Tsuchiya, C. Horikoshi, and T. Sato, "On the spread of rectangular jets," Exp. Fluids **4**, 197 (1986).
[10] Y. Tsuchiya, C. Horikoshi, T. Sato, and M. Takahashi, "A study on the spread of rectangular jets (The mixing layer near the jet exit and visualization by the dye method)," JSME Int. J., Ser. II **32**, 11 (1989).
[11] W. R. Quinn and J. Militzer, "Experimental and numerical study of a turbulent free square jet," Phys. Fluids **31**, 1017 (1988).
[12] W. R. Quinn, "Passive near-field mixing enhancement in rectangular jet flows," AIAA J. **4**, 515 (1991).
[13] W. R. Quinn, "Turbulent free jet flows issuing from sharp-edged rectangular slots: The influence of slot aspect-ratio," Exp. Therm. Fluid Sci. **5**, 203 (1992).
[14] W. R. Quinn, "Development of a large-aspect-ratio rectangular turbulent free jet," AIAA J. **32**, 547 (1994).
[15] W. R. Quinn, "Turbulent mixing in a free jet issuing from a low aspect ratio contoured rectangular nozzle," Aeronaut. J. **2110**, 337 (1995).
[16] M. Lozanova and P. Stankov, "Experimental investigation on the similarity of a 3D rectangular turbulent jet," Exp. Fluids **24**, 470 (1998).
[17] A. Krothapalli, D. Baganoff, and K. Karamcheti, "On the mixing of a rectangular jet," J. Fluid Mech. **107**, 201 (1981).
[18] G. B. Van Der Hegge Zijen, "Measurements of the velocity distribution in a plane turbulent jet of air," Appl. Sci. Res., Sect. A **7**, 256 (1958).
[19] S. Koshigoe and A. Tubis, "Wave structure in jets of arbitrary shape. I. Linear inviscid spatial instability analysis," Phys. Fluids **29**, 3982 (1986).
[20] S. Koshigoe and A. Tubis, "Wave structure in jets of arbitrary shape. II. Application of a generalized shooting method to linear stability analysis," Phys. Fluids **30**, 1715 (1987).
[21] C. K. W. Tam and A. T. Thiess, "Instability of rectangular jets," J. Fluid Mech. **248**, 425 (1993).
[22] F. F. Grinstein, "Self-induced vortex ring dynamics in subsonic rectangular jets," Phys. Fluids **7**, 2519 (1995).
[23] F. F. Grinstein, "Vortex dynamics and entrainment in rectangular free jets," J. Fluid Mech. **437**, 69 (2001).
[24] R. S. Miller, C. K. Madnia, and P. Givi, "Numerical simulation of non-circular jets," Comput. Fluids **24**, 1 (1995).
[25] R. V. Wilson and A. O. Demuren, "Numerical simulation of turbulent jets with rectangular cross-section," J. Fluids Eng. **120**, 285 (1998).
[26] B. Rembold, N. A. Adams, and L. Kleiser, "Direct numerical simulation of a transitional rectangular jet," Int. J. Heat Fluid Flow **23**, 547 (2002).
[27] H. Feiz, J. H. Soo, and S. Menon, "LES of turbulent jets using the lattice Boltzmann approach," 41st AIAA Aerospace Sciences Meeting and Exhibit, AIAA-03-0780, Reno, NV, 6–9 January 2003.
[28] G. McNamara and G. Zanetti, "Use of the Boltzmann equation to simulate lattice-gas automata," Phys. Rev. Lett. **61**, 2332 (1988).
[29] F. J. Higuera and J. Jiménez, "Boltzmann approach to lattice gas simulations," Europhys. Lett. **9**, 663 (1989).
[30] R. Benzi, S. Succi, and M. Vergassola, "The lattice Boltzmann equation: Theory and applications," Phys. Rep. **222**, 145 (1992).
[31] S. Chen and G. D. Doolen, "Lattice Boltzmann method for fluid flows," Annu. Rev. Fluid Mech. **30**, 329 (1998).
[32] L.-S. Luo, "The lattice-gas and lattice Boltzmann methods: Past, present and future," in *Proceedings of the International Conference on Applied CFD, Beijing*, edited by J.-H. Wu and Z.-J. Zhu (ICAC2002 publication, Beijing, 2000), pp. 52–83.
[33] D. Yu, R. Mei, L.-S. Luo, and W. Shyy, "Viscous flow computations with the method of lattice Boltzmann equation," Prog. Aerosp. Sci. **39**, 329 (2003).
[34] H. Yu, S. S. Girimaji, and L.-S Luo, "DNS and LES of decaying homogeneous isotropic turbulence with and without system rotations using lattice Boltzmann method," J. Comput. Phys. **209**, 599 (2005).
[35] H. Chen, S. Chen, and W. H. Matthaeus, "Recovery of the Navier-Stokes equations using a lattice-gas Boltzmann method," Phys. Rev. A **45**, R5339 (1992).
[36] Y. Qian, D. d'Humiéres, and P. Lallemand, "Lattice BGK models for Navier-Stokes equation," Europhys. Lett. **17**, 479 (1992).
[37] D. d'Humiéres, "Generalized lattice-Boltzmann equations." in *Rarefied Gas Dynamics: Theory and Simulations*, Prog. Aeronaut. Astronaut. Vol. 159, edited by B. D. Shizgal and D. P. Weaver (AIAA, Washington, D. C., 1992), pp. 450–458.
[38] P. Lallemand and L.-S. Luo, "Theory of the lattice Boltzmann method: Dispersion, dissipation, isotropy, Galilean invariance, and stability," Phys. Rev. E **61**, 6546 (2000).
[39] D. d'Humiéres, I. Ginzburg, M. Krafczyk, P. Lallemand, and L.-S. Luo, "Multiple-relaxation-time lattice Boltzmann models in three dimensions," Proc. R. Soc. London, Ser. A **360**, 437 (2002).
[40] I. Ginzburg and D. d'Humiéres, "Multireflection boundary conditions for lattice Boltzmann models," Phys. Rev. E **68**, 066614 (2003).
[41] H. Yu, L.-S. Luo, and S. S. Girimaji, "Implementation of MRT lattice Boltzmann method for large eddy simulation of turbulent flows," Comput. Fluids (in press).
[42] L.-S. Luo, "Theory of the lattice Boltzmann method: Lattice Boltzmann models for nonideal gases," Phys. Rev. E **62**, 4982 (2000).
[43] T. S. Chyczewski, L. N. Long, and P. J. Morris, "Numerical study of nozzle exit condition effects on jet development," AIAA J. **36**, 986 (1998).
[44] H. Yu, S. S. Girimaji, and L.-S. Luo, "Lattice Boltzmann simulations of decaying homogeneous isotropic turbulence with and without system rotation," Phys. Rev. E **71**, 204501 (2005).
[45] D. Yu and S. S. Girimaji, "DNS of homogeneous shear turbulence revisited with the lattice Boltzmann method," J. Turbul. **6**, 1 (2005).
[46] P. L. Bhatnagar, E. P. Gross, and M. Krook, "A model for collision processes in gases. I. Small amplitude processes in charged and neutral one-component systems," Phys. Rev. **94**, 511 (1954).
[47] X. He and L.-S. Luo, "Lattice Boltzmann model for the incompressible Navier-Stokes equation," J. Comput. Phys. **88**, 927 (1997).
[48] S. B. Pope, *Turbulent Flows* (Cambridge University Press, Cambridge, 2000).
[49] J. Smagorinsky, "General circulation experiments with the primitive equations: I. The basic equations," Mon. Weather Rev. **91**, 99 (1963).
[50] S. Hou, J. Sterling, S. Chen, and G. D. Doolen, "A lattice Boltzmann subgrid model for high Reynolds number flows," in *Pattern Formation and Lattice Gas Automata*, Fields Inst. Comm., Vol. 6, edited by A. T. Lawniczak and R. Kapral (AMS, Providence, 1996), pp. 151–166.
[51] G. Zanetti, "Hydrodynamics of lattice-gas automata," Phys. Rev. A **40**, 1539 (1989).
[52] H. Yu and S. S. Girimaji, "Lattice Boltzmann equation simulation of rectangular jet (AR=1.5) instability and axis-switching," Physica A (in press).